

rt-TDDFT modeling of thermal emission by laser-heated glasses

Grigory Kolesov

Corning Inc., Painted Post, New York, USA

(Dated: January 15, 2025)

In the laser processing of glass, a $\sim 50\text{-}1000\ \mu\text{m}$ -thick layer of glass is heated to a high temperature by the laser beam. Due to the shallow depth of this hot layer, the infrared emission and absorption spectra may deviate from the black-body spectra and can be influenced by the vibrational structure of the material. Real-time time-dependent density functional theory (rt-TDDFT) modeling of the thermal radiation by such hot layers allows us to calculate the emissivity and thus to evaluate the reliability of the measurements conducted with thermal cameras at specific wavelengths.

INTRODUCTION

Accurate measurements of temperature of glasses close to the softening point ($T \sim 1000 - 2000\ \text{K}$) require the knowledge of emissivity at the wavelengths used by the thermal camera, which are typically in the $4\text{-}8\ \mu\text{m}$ (mid-wavelength infrared, MWIR) and $8\text{-}14\ \mu\text{m}$ (long-wavelength infrared, LWIR) ranges. Because in the laser processing of glasses, the laser-heated region can be arbitrarily thin, the emissivity, especially in the MWIR range, can be diminished and calibration procedures performed on the bulk glass can be invalidated.

Density functional theory (DFT) simulations can provide accurate information about the infrared response, absorption, and emission of the material. To account for anharmonism and finite temperatures, the molecular dynamics (MD) Green-Kubo approach was developed¹⁻³. One difficulty with this method is that the dipole moment is ill-defined in the periodic boundary conditions, which are most suited for simulations of glass. This difficulty was overcome through the development of the modern theory of polarization^{4,5}. With its use, the infrared response was previously computed with the Green-Kubo approach in Refs.^{2,3} via calculation of maximally-localized Wannier orbitals. Below, we demonstrate another approach which, within real-time time-dependent DFT (rt-TDDFT), directly computes the change of the macroscopic polarization as the total current through the simulation cell. We also test simplified approaches based on charge partitioning schemes.

I. MATERIALS AND METHODS

In this work, our objective is to calculate the emission and absorption of IR radiation by glass at high temperature close to the softening point. Additionally, the OH (hydroxyl) emission and absorption band is of particular interest.

In order to make a comparison with experimental data it is useful to calculate the spectral radiance L :

$$L(\omega, T) = \frac{\hbar\omega^3}{4\pi^3c^2} \frac{1 - e^{-\alpha(\omega)d}}{e^{\frac{\hbar\omega}{k_B T}} - 1}, \quad (1)$$

where α is the Napierian absorption coefficient and d is

the thickness of the emitting layer (see Appendix A for relations between different absorption coefficients). In this work, a hot layer of uniform temperature is considered for simplicity.

The IR light is absorbed in the material through vibrational excitation of atomic dipoles. The quantum dipole-dipole autocorrelation function and its Fourier transform can be approximately computed via the classical autocorrelation function¹:

$$\begin{aligned} & \int_{-\infty}^{\infty} dt e^{-i\omega t} \langle \frac{1}{2} [\hat{\boldsymbol{\mu}}(0), \hat{\boldsymbol{\mu}}(t)]_+ \rangle \\ &= \frac{\beta\hbar\omega}{2} \coth\left(\frac{\beta\hbar\omega}{2}\right) \int_{-\infty}^{\infty} dt e^{-i\omega t} \langle \boldsymbol{\mu}(0) \cdot \dot{\boldsymbol{\mu}}(t) \rangle_{\text{cl}}, \quad (2) \end{aligned}$$

where $[\]_+$ denotes the anticommutator, $\boldsymbol{\mu}$ is the total dipole moment of the system, $\hat{\boldsymbol{\mu}}$ is the dipole moment operator and $\beta = 1/k_B T$.

The imaginary part $\varepsilon_2(\omega)$ of the dielectric function can be found via Green-Kubo relation for the dipole or dipole time-derivative autocorrelation function²:

$$\varepsilon_2(\omega) = \frac{\beta}{6V\omega\varepsilon_0} \int_{-\infty}^{\infty} dt e^{-i\omega t} \langle \dot{\boldsymbol{\mu}}(0) \cdot \dot{\boldsymbol{\mu}}(t) \rangle_{\text{cl}}, \quad (3)$$

where V is the system's volume and the dot indicates the time-derivative. The time-derivative form of the relation is chosen for numerical efficiency.

The real part of the dielectric function $\varepsilon_1(\omega)$ is obtained from the Kramers-Krönig relation:

$$\varepsilon_1(\omega) - 1 = \frac{2}{\pi} \mathcal{P} \int_0^{\infty} \frac{\omega' \varepsilon_2(\omega')}{\omega'^2 - \omega^2} d\omega', \quad (4)$$

with \mathcal{P} indicating Cauchy principal value. Eq. (4) can either be evaluated via direct numerical integration, or by taking two successive Fourier transforms^{2,6}:

$$\varepsilon_1(\omega) - 1 = \frac{2}{\pi} \int_0^{\infty} \int_0^{\infty} \varepsilon_2(\omega') \sin(\omega'\tau) \cos(\omega\tau) d\omega' d\tau \quad (5)$$

In the periodic boundary conditions used in the calculations below the dipole moment is not defined. One way to deal with this problem is to use localized Wannier functions^{2,3,7}. However, this requires finding localized Wannier functions at each MD time step. Another approach, which we propose here, is to directly calculate

the autocorrelation function for the time derivative of the macroscopic polarization $\mathbf{P}(t)$, which is the total current through the simulation cell^{4,5,7}:

$$\mathbf{P}(t) = \frac{1}{V_{\text{cell}}} \int_0^t \mathbf{j}_{\text{cell}}(t') dt'. \quad (6)$$

\mathbf{j}_{cell} can be calculated either directly in real-time time-dependent DFT (rt-TDDFT, Method 1) or by calculation of the partial charges on atoms and multiplying them by the atomic velocity vectors (Method 2).

Numerical simulations. We used the SIESTA⁸ DFT code with certain modifications implemented by us, including rt-TDDFT⁹. We used the PBE exchange-correlation functional¹⁰ and the double- ζ +polarization (DZP) basis set. We found that this higher-accuracy basis is necessary to correctly reproduce the frequency of the OH stretch vibration.

A fused-silica simulation cell was prepared by simulated annealing at constant volume for 20 ps. The resulting simulation cell contained 95 atoms including two hydroxyl groups. We used a time step of 0.3 fs in all our standard (adiabatic) molecular dynamics simulations. Such a reduced time step is necessary to capture motion of the hydrogen atom. In the rt-TDDFT calculations we used a time step of 1 a.u. (≈ 24 as). In order to obtain the realistic concentration of OH we also calculated the absorption spectrum for the fused-silica cell with no OHs and then calculated the weighted average of the two spectra with weights made to match the experimental OH concentration.

We used the Hirshfeld and Bader charge partitioning methods for the partial charge-based method (Method 2). We also tested the Voronoi deformation density charge partitioning scheme¹¹, however the results of this scheme were very similar to those obtained with the Hirshfeld method, so only the latter is reported here. Bader charges were calculated with *Bader* code¹².

II. RESULTS AND DISCUSSION

A. Fused silica.

Table I presents the absorption coefficients for the peak OH band absorption. The Hirshfeld charge-based method (Method 2) and the rt-TDDFT method (Method 1) both are in good agreement with the experimental measurements. Both methods overestimate the absorption somewhat, but in both cases it is quite close to the measurement by Williams *et al.*¹⁴. Note that Method 1 derives the absorption spectrum from the calculation, which is accurate within the simulation, while Method 2 is an approximate way of extracting absorption from the simulation. However it utilizes more trajectory data points due to the low cost of each MD time step in adiabatic DFT simulations.

Note that the effect of peak broadening due to configurational disorder is not explored in this work; we cal-

culate the absorption exactly at the peak. Thus, there is some uncertainty associated with the calculated values presented in Table I. Ideally, we would conduct many simulations on different SiO₂ + OH configurations and then average the resulting spectra.

Figs. 1 (Method 1) and 2 (Method 2) present a more integral way of comparing the results to the experiment. Fig. 1a shows the spectral radiance of the 6mm 0.15 weight-% OH fused silica sample at $T = 1600$ K. In order to average out the discrete peaks resulting from the finite-size simulation cell (the thin blue line on Fig. 1a) we applied low-pass filter (the thick purple line). This smoothed-out version of the spectral radiance was then used to calculate the emissivity (Fig. 1b). The experimental emissivity curve ($T = 1675$ K) measured by Dvurenchsky *et al.*¹³ is shown as the dashed orange line in Fig. 1b. The agreement between the simulation and the experiment is good. The OH-peak is slightly red-shifted, but otherwise it is where it should be and has a correct width. The emissivity is dropping off from the black-body value at $\sim 4 \mu\text{m}$ both in the experiment and the simulation. The overlap between OH-peak and the tail of the black-body emission is also in agreement. The satellite (combination) peak at $\sim 2.3 \mu\text{m}$ is reproduced well. It is also slightly red-shifted, but its intensity and width agree with the experiment within the uncertainty of the simulation (the thin blue line in Fig. 1a).

The simulation results show a peak in the emissivity at low wavelengths. It corresponds to the electronic excitations, which are also captured by the rt-TDDFT method. It is indistinguishable from zero on the absolute scale (Fig. 1a) and is not seen in the experiment, as it is out of the spectrometer range.

The results of the calculation with Method 2 and Hirshfeld charges for a 6mm-thick sample are shown in Fig. 2. The OH-peak and the combination mode peak at $2.3 \mu\text{m}$ are captured well with this method. The OH-overtone mode at $\sim 1.4 \mu\text{m}$ is clearly seen in Fig. 2b. However the drop-off from the black-body behavior starts at too large a wavelength $\sim 5.5 \mu\text{m}$, resulting in the local minimum of the emissivity (0.7) at $4 \mu\text{m}$. Evidently, bulk silica dipoles are not represented well with this method, resulting in the overall poor emission and absorption prediction. This is possibly due to the underestimation of partial charges on ions in more covalent Si-O bonds, but correct charge assignments in polar O-H bond with the Hirshfeld charge partitioning scheme.

Fig. 2 also shows the spectrum and spectral emissivity calculated with Bader charges. Typically, Bader charge partitioning results in near-integer charges consistent with the oxidation state of an ion. In the simulations presented here, Bader charges significantly overestimate the actual effective charges, which results in the incorrect, nearly black-body emission spectrum.

This assessment of Hirshfeld, Voronoi and Bader charges broadly agrees with the conclusions of Ref.¹¹.

One of the goals of this calculation is to understand thermal-camera measurements in laser processing

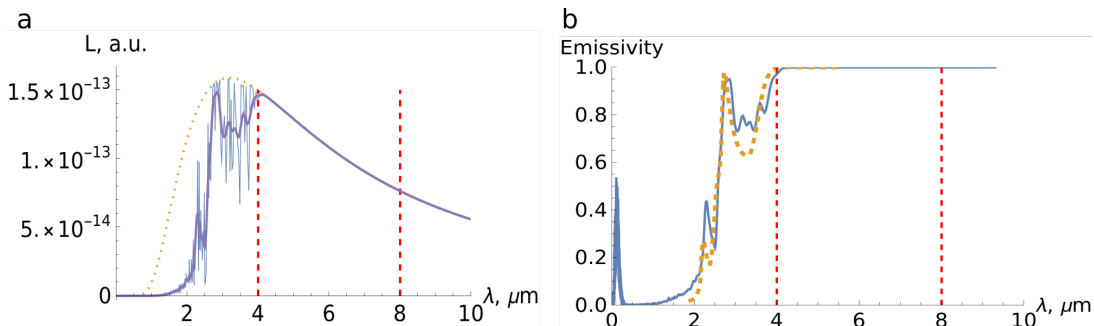


FIG. 1. Method 1: The calculated emission spectra (a) and the spectral emissivity (b), for a 6mm-thick, 0.15 weight-% OH fused silica sample at $T = 1600$ K. In (a) the orange dotted line shows the black-body emission spectrum, the thin blue line shows the calculated emission spectrum while the purple line shows the smoothed version of the calculated spectrum. The latter was used to calculate (b). In (b) the solid blue line shows the calculated spectral emissivity and the dashed orange line shows the experimental curve from Ref.¹³. In both plots the red dashed lines mark the wavelengths range between $4 \mu\text{m}$ and $8 \mu\text{m}$ often used by thermal cameras.

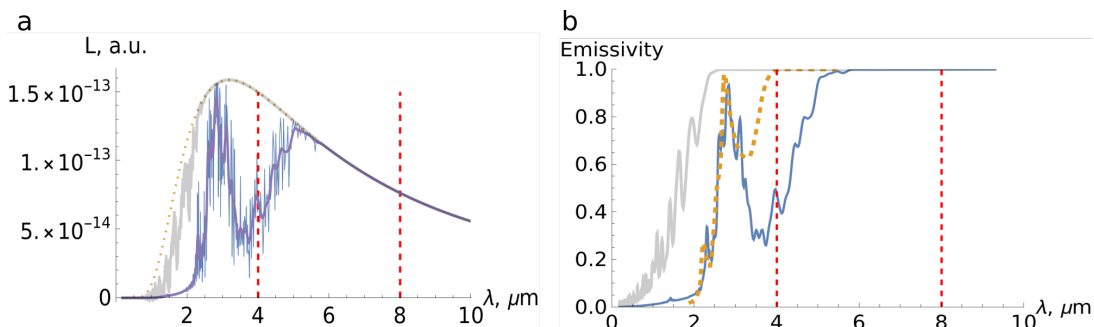


FIG. 2. Method 2: The calculated emission spectra (a) and the spectral emissivity (b), for a 6mm-thick, 0.15 weight-% OH fused silica sample at $T = 1600$ K. In (a) the orange dotted line shows the black-body emission spectrum, the thin blue line shows the calculated emission spectrum (Hirshfeld charge method) while the purple line shows the smoothed version of the calculated spectrum. The thick gray line shows the spectrum calculated with Bader charges. In (b) the solid blue line (Hirshfeld charge method, smoothed) and thick gray line (Bader charge method) show the calculated spectral emissivity. The dashed orange line shows the experimental curve from Ref.¹³.

of glass. In the laser processing the heated region does not necessarily extend through the whole sample and can be arbitrarily thin. The effect of the heated-region thickness is explored in Fig. 3 for 1000-ppm OH fused silica (similar in OH-content to the Corning-made HPFS).

The temperature measurement at $4 \mu\text{m}$ would be unreliable even for the 1 mm sample, where the $4 \mu\text{m}$ line falls right onto the step-like transition between the black-body and the structured radiation. It should be noted that the calculation uncertainty is very high at $4 \mu\text{m}$ (as seen from the non-smoothed calculation curve depicted by the thin blue line in Fig. 3a). The emissivity at $4 \mu\text{m}$ is significantly lower than 1 for the 0.5 mm and 0.1 mm thicknesses, approximately 0.45 and 0.15, respectively. The temperature measurement at $8 \mu\text{m}$ would be reliable in all cases.

OH-stretch overtone

It is interesting to see that in the emission spectra calculated with Hirshfeld charges, the OH-vibration overtone peak at about $1.4 \mu\text{m}$ is easily seen. Since this peak is of particular importance in optical fibers, it was investigated further.

Fig. 4 presents the absorption coefficient at $T = 1600$ K in the customary units of dB/km/ppm calculated with both methods. The overtone peak is seen with both methods, although with Method 1 it is barely distinguishable from the background absorption, possibly resulting from the thermal broadening of the $2.3 \mu\text{m}$ combination peak. With both methods the height of the peak is significantly below the room-temperature value¹⁵. With Method 1, however the peak height could be consistent with the temperature-dependence trend observed in the Ref.¹⁶, where the peak intensity at $T = 500$ K was measured to be significantly below the room-temperature value. With Method 2, the peak is more distinct, but it is significantly red-shifted and lower in intensity than the

	Ref ¹⁴	Ref ¹³	rt-TDDFT (this work, Method 1)	DFT (this work, Method 2)
α , cm^{-1} (10^3 weight-ppm OH)	12.83	9.87	14.45	13.66
ϵ_{10} , $\text{L cm}^{-1}/\text{mol}$	43	33.1	48.44	45.78
σ , 10^{-19} cm^2	1.64	1.27	1.85	1.75
Peak wavelength, μm	2.73	2.72	2.79	2.85

TABLE I: Experimental and theoretical OH-band peak absorption coefficients for fused silica.

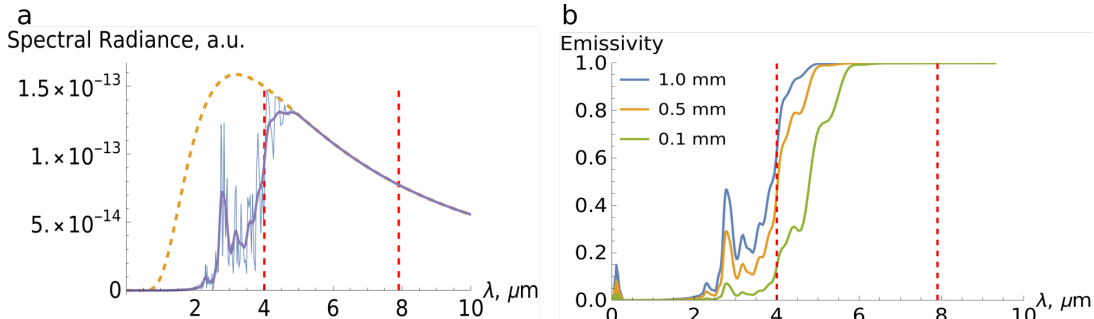


FIG. 3. The effect of the heated region thickness on the emissivity for the 1000-ppm OH-content HPFS glass. The calculated emission spectra for the 1 mm-thick heated region (a) and the spectral emissivity (b) for the 1 mm (blue curve), 0.5 mm (orange) and 0.1 mm (green)-thick heated regions. In (a) the orange dotted line shows the black-body emission spectrum, the thin blue line shows the calculated emission spectrum, and the purple line shows the smoothed version of the calculated spectrum. In both plots the red dashed lines mark the wavelengths range between $4 \mu\text{m}$ and $8 \mu\text{m}$ often used by thermal cameras.

room-temperature value.

To clarify this further, the absorption spectrum at $T = 300 \text{ K}$ was calculated with Method 1. The overtone peak was present, but it was two orders of magnitude below the experimental value. Clearly for such a high frequency ($\lambda = 1.4 \mu\text{m}$, $\omega = 0.9 \text{ eV} = 10277 \text{ K}$), the assumptions behind the quantum-classical equivalence Eq. (2) are not satisfied. In this classical-ion simulation the temperature on energy scale was much lower than the frequency of the OH-stretch mode, resulting in only a slight excitation of the mode and limited exploration of the anharmonic part of the potential. This is in contrast to a quantum oscillator, which is half-excited in the zeroth state.

Therefore, the Green-Kubo-based method is unreliable for high-frequency vibrational overtones due to the failure of quantum-classical equivalence for high-frequency vibrations, which are in the quantum zero-point regime.

B. Borofloat

To explore the technique developed in this work on more complex glass we created the simulation cell for the Borofloat glass. The composition of Borofloat was taken from the BOROFLOAT[®] 33 specification web page and is, in mol-%, 81% SiO_2 , 13% B_2O_3 , 4% $\text{Na}_2\text{O}/\text{K}_2\text{O}$, 3% Al_2O_3 . We added 1% of OH molecules into the composition and adjusted the content of the other oxides accordingly. The resulting simulation cell had about 200 atoms. We applied rt-TDDFT at $T = 1050 \text{ K}$ to calculate the IR absorption and emission. The results for the 0.1 mm-thick heated region are presented in Fig. 5.

The 0.1 mm thickness was chosen so that the spectrum structure around $4 \mu\text{m}$ would be visible.

The main OH-peak and the $2.3 \mu\text{m}$ combination peak are again clearly distinguishable. At room temperature the transmission spectrum for 2000 ppm OH-content matches reasonably well given the uncertainty in the composition and finite size effects to the transmission spectrum measured by Schott (Fig. 6).

III. CONCLUSIONS

The Green-Kubo approach, in combination with rt-TDDFT, was used to calculate the absorption and emission of glasses at high-temperature, close to the softening point. The autocorrelation functions of the total current were transformed to obtain the IR response at a given temperature. Good agreement with the experimental measurements was observed for fused silica. The OH-band, with its satellite peaks, which is of particular importance for this study, was well reproduced.

A multi-component glass, BOROFLOAT[®] 33, was also considered in this work. The simulation reproduced the transmission spectrum provided in the BOROFLOAT[®] 33 specification well, given the uncertainty in the exact composition and finite size effects.

All simulations demonstrated the risk associated with temperature measurements of the laser-heated spots using the IR camera that operates below $6 \mu\text{m}$ wavelengths. For these wavelengths, measurements calibrated on thick glass samples may not accurately reflect the temperature of the thin laser-heated region due to its lower emissivity.

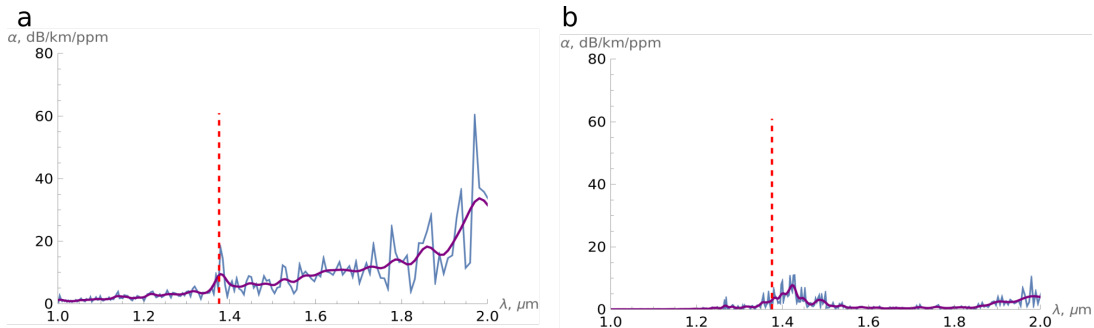


FIG. 4. The absorption coefficient in the conventional dB/km/ppm units around the 1.4 μm wavelength ($T = 1600$ K). (a) Calculated with Method 1 and (b) with Method 2. In both plots blue curve is the calculated absorption coefficient, thick purple line is the smoothed version and red dashed line indicates OH-overtone peak position and height at room temperature¹⁵.

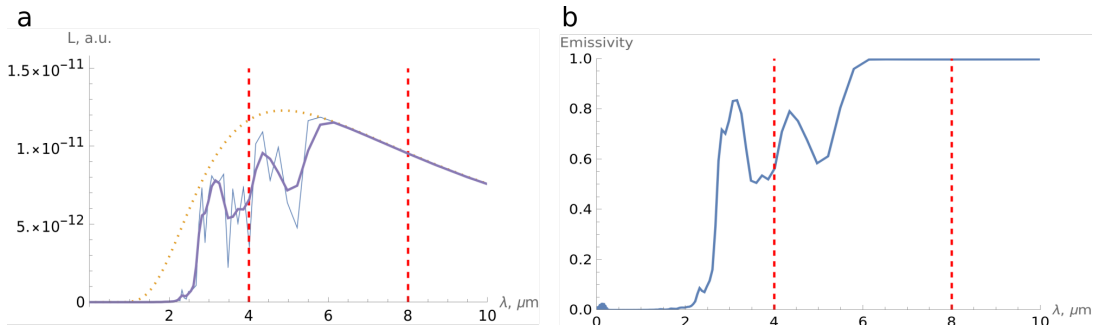


FIG. 5. The calculated emission spectra (a) and the spectral emissivity (b), for a 100 μm -thick, 1 weight-% OH Borofloat sample at $T = 1050$ K. In (a) the orange dotted line shows the black-body emission spectrum, the thin blue line shows the calculated emission spectrum and the purple line shows the smoothed version of the calculated spectrum. The latter was used to calculate (b). In (b) the solid blue line shows the calculated spectral emissivity.

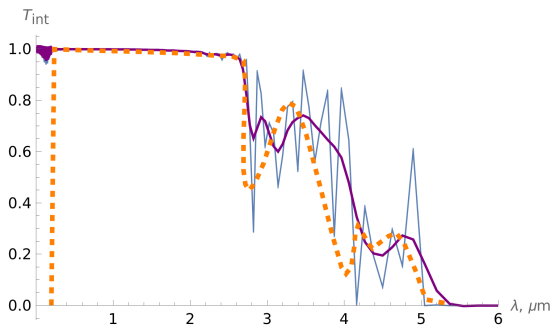


FIG. 6. The transmission spectrum of 0.2 mm-thick BOROFLOAT[®] 33 at room temperature. The orange dashed curve shows the experimental transmission spectrum from the BOROFLOAT[®] 33 specification webpage (digitized and normalized to be 1 at the maximum of transmission). Purple thick line shows the smoothed version of the calculated transmission spectrum at $T = 300$ K and 2000 ppm OH-content, while the original non-smoothed spectrum is shown with the thin blue line.

For very high frequency vibrational bands, in particular OH overtone band, the method was not able to accurately reproduce the peak intensity, although the peak position was reasonably accurate. This is because for

high frequency vibrations, even at temperatures around the softening point, the vibrational state is in the quantum zero-point regime which is not reproduced well in the quantum-to-classical mapping used in the classical MD-based Green-Kubo approach used in this work.

When we attempted to simplify the calculation of the total current by using Hirshfeld or Voronoi partial charges, the method was not able to accurately reproduce the experimental IR emission. Interestingly, while the OH-band was relatively well reproduced, the emission related to the top of the SiO₂ band was poorly reproduced. We deduce that Hirshfeld and Voronoi partial charge methods work well for highly polar bonds, such as OH-bonds, but fail for less polar bonds, such as Si-O. Bader charge partitioning scheme resulted in overestimation of the emission intensities and nearly black-body emission that drowned all of the structured signal. Thus, IR emission and absorption spectra serve as useful benchmark to assess the applicability of the charge partitioning schemes.

ACKNOWLEDGEMENTS

The author is grateful to Dr. Alex Streltsov for introduction to the problem and many fruitful discussions, and to Dr. Douglas Allan for thorough reading and providing feedback on the manuscript.

Appendix A: Relations between different optical constants

The average rate of absorption of energy E per light absorber is given by

$$\frac{\partial E}{\partial t} = \sigma I, \quad (\text{A1})$$

where I is the light intensity (power per unit area) and σ is the absorption cross-section. σ is related to the molar absorption coefficient ϵ through

$$\sigma = \epsilon/N_A, \quad (\text{A2})$$

where N_A is the Avogadro constant.

The absorption coefficient α and the molar absorption coefficient ϵ are related through the molar concentration q of the absorbing species:

$$\alpha = q \cdot \epsilon \quad (\text{A3})$$

The Napierian α , ϵ (base-e) and the decadic α_{10} , ϵ_{10} (base-10) absorption coefficients are related by the log-factor:

$$\begin{aligned} \alpha_{10} &= \alpha / \log 10 \\ \epsilon_{10} &= \epsilon / \log 10, \end{aligned} \quad (\text{A4})$$

where \log indicates the Napierian logarithm.

The Napierian α , measured in cm^{-1} , is converted to dB/km/ppm units with

$$\alpha_{\text{dB}} = \alpha 10^6 \log_{10} e / q_{\text{ppm}}, \quad (\text{A5})$$

where q_{ppm} is the concentration of the absorbing species in ppm.

Frequency-dependent absorption coefficient $\alpha(\omega)$ is related to the complex refractive index $\hat{n}(\omega)$ and complex dielectric function $\varepsilon(\omega)$:

$$\begin{aligned} \varepsilon(\omega) &= \varepsilon_1(\omega) + i\varepsilon_2(\omega) \\ \hat{n}(\omega) &= n(\omega) + ik(\omega) \\ \varepsilon(\omega) &= \hat{n}^2 \\ \alpha(\omega) &= \frac{2\omega}{c}k(\omega) \\ \varepsilon_2(\omega) &= \frac{c}{\omega}\alpha(\omega)n(\omega), \end{aligned} \quad (\text{A6})$$

where ε_1 and ε_2 are real and imaginary parts of the complex dielectric function, and $n(\omega)$ and $k(\omega)$ are real and imaginary part of the complex refractive index. (Magnetic permeability μ is assumed to be unity.)

REFERENCES

-
- ¹ Bader, J. S. & Berne, B. Quantum and classical relaxation rates from classical simulations. *J. Chem. Phys.* **100**, 8359–8366 (1994). 1
- ² Iftimie, R. & Tuckerman, M. E. Decomposing total ir spectra of aqueous systems into solute and solvent contributions: A computational approach using maximally localized wannier orbitals. *J. Chem. Phys.* **122**, 214508 (2005). 1
- ³ Thomas, M., Brehm, M., Fligg, R., Vöhringer, P. & Kirchner, B. Computing vibrational spectra from ab initio molecular dynamics. *Phys. Chem. Chem. Phys.* **15**, 6608–6622 (2013). 1
- ⁴ Resta, R. Theory of the electric polarization in crystals. *Ferroelectrics* **136**, 51–55 (1992). 1, 2
- ⁵ King-Smith, R. & Vanderbilt, D. Theory of polarization of crystalline solids. *Phys. Rev. B* **47**, 1651 (1993). 1, 2
- ⁶ Frohlich, H. *Theory of Dielectrics: Dielectric Constant and Dielectric Loss* (Oxford University Press, 1949), 1st edition edn. 1
- ⁷ Resta, R. & Vanderbilt, D. Theory of polarization: a modern approach. In *Physics of ferroelectrics: a modern perspective*, 31–68 (Springer, 2007). 1, 2
- ⁸ Soler, J. M. *et al.* The SIESTA method for *ab initio* order-N materials simulation. *J. Phys.: Condens. Matter* **14**, 2745 (2002). 2
- ⁹ Kolesov, G., Grånäs, O., Hoyt, R., Vinichenko, D. & Kaxiras, E. Real-time TD-DFT with classical ion dynamics: Methodology and applications. *J. Chem. Theory Comput.* **12**, 466–476 (2016). 2
- ¹⁰ Perdew, J. P., Burke, K. & Ernzerhof, M. Generalized gradient approximation made simple. *Phys. Rev. Lett.* **77**, 3865 (1996). 2
- ¹¹ Fonseca Guerra, C., Handgraaf, J.-W., Baerends, E. J. & Bickelhaupt, F. M. Voronoi deformation density (VDD) charges: Assessment of the Mulliken, Bader, Hirshfeld, Weinhold, and VDD methods for charge analysis. *J. Comput. Chem.* **25**, 189–210 (2004). 2
- ¹² Tang, W., Sanville, E. & Henkelman, G. A grid-based Bader analysis algorithm without lattice bias. *J. Phys.: Condens. Matter* **21**, 084204 (2009). 2
- ¹³ Dvurechensky, A., Petrov, V. & Reznik, V. Y. Spectral emissivity and absorption coefficient of silica glass at extremely high temperatures in the semitransparent region. *Infrared Physics* **19**, 465–469 (1979). 2, 3, 4
- ¹⁴ Williams, J. P. *et al.* Direct determination of water in glass. *Ceramic Bull.* **55**, 524–527 (1976). 2, 4
- ¹⁵ Humbach, O., Fabian, H., Grzesik, U., Haken, U. & Heitmann, W. Analysis of oh absorption bands in synthetic silica. *Journal of non-crystalline solids* **203**, 19–26 (1996). 3, 5
- ¹⁶ Yu, L. *et al.* Observation of temperature dependence of the ir hydroxyl absorption bands in silica optical fiber. *Optical Fiber Technology* **30**, 1–7 (2016). 3